

Matildite Contact with Media: First-Principles Study of AgBiS₂ Surfaces and Nanoparticle Morphology

Francesc Viñes,¹ Gerasimos Konstantatos,^{2,3} and Francesc Illas^{1,*}

¹*Departament de Ciència de Materials i Química Física & Institut de Química Teòrica i Computacional (IQTCUB), Universitat de Barcelona, C/Martí i Franquès 1, 08028 Barcelona, Spain.*

²*ICFO-Institut de Ciències Fotòniques. The Barcelona Institute of Science and Technology, 08860 Castelldefels (Barcelona), Spain.*

³*ICREA-Institució Catalana de Recerca i Estudis Avançats. Passeig Lluís Companys 23, 08010 Barcelona, Spain.*

Abstract

Motivated by the interest in AgBiS₂ material for solar light harvesting applications, a detailed bulk first principles quantum mechanical of surface properties is presented. Density functional theory based calculations with the Perdew-Burke-Ernzerhof functional have been carried out for different surface orientations and terminations of its matildite polymorph. From the results, two particularly stable facets are predicted to dominate Wulff shaped AgBiS₂ nanoparticles. These are the (001) type nonpolar surface and the (111) polar terminations where facets are exposed containing solely Ag or S atoms. The Wulff equilibrium shape is predicted to be a cube with only two edges capped. This particular shape explains a previously reported surface enrichment of Ag with respect Bi of ~1.5. The (001) surfaces display an ionic character similar to bulk AgBiS₂, with a low work function of 4.31 eV, although the inspection of the density of states (DOS) reveals a bandgap increased by 0.3 eV compared to bulk. This surface effect could explain the bulk wavelength overestimation of the absorption coefficient decay, as previously determined. Last but not least, the DOS of (111) polar termination reveals a metallic character, where Fermi level is located below that on the (001) surfaces. Possible implications of the different electronic structure of these surfaces in the reported photoactivity are discussed.

* Corresponding author: francesc.illas@ub.edu

1. Introduction

Silver-Bismuth sulphur (AgBiS_2) has recently been the focus of much research attention since its nanoparticles can be used in high-performance solar cells.¹ Aside, it has been appointed as a sensitizer and/or counter-electrode in sensitized solar cells,^{2,3} plus its ultralow thermal conductivity enables the use in thermoelectric power generation.^{4,5} Matildite renewed interest goes along other materials of the I-V-VI₂ family —I = Cu, Ag, or an alkali metal; V = Sb or Bi; VI = S, Se, or Te— lately studied also for solar cells,^{1,6} but well considered in addition in thermoelectrics^{4,7} and phase-change memory devices.^{8,9}

A recent thorough fundamental study based on density functional (DF) theory¹⁰ showed that the origin of the high photoactivity of AgBiS_2 is linked to the existence of its Matildite polymorph —Pearson symbol $hP12$ and space group 164, *i.e.* $P\bar{3}m1$ —, and specifically to the different effective masses of excited electrons in the conduction band and the generated electron holes in the valence band, plus a high dielectric constant^{10,11} and a large absorption coefficient.¹⁰ However, it is worth pointing out that, for the above-commented applications, AgBiS_2 colloidal nanocrystals are used with 4.62 ± 0.97 nm size¹ with a large surface/bulk ratio. Note also that even when employing larger size nanoparticles, such as the ~ 16 nm particles in sensitized solar cells,⁶ the surface region is directly in contact with media. Hence, surfaces are likely to play a paramount role in carrier transport and recombination as in the solution processed AgBiS_2 based solar cells.¹ A similar situation is found for the grains of ~ 50 nm as detected in AgBiS_2 thin films by means of atomic force microscopy (AFM).¹² Therefore, a thorough theoretical study on AgBiS_2 matildite surfaces and possible nanoparticle shape is mandatory, in order to rationalize and better interpret past and future research on matildite, a piece of the puzzle which is, hitherto, inexistent.

Regarding the available information of the different surfaces of matildite, previous high-resolution transmission electron microscopy (HR-TEM) experiments on AgBiS_2 reveal a preferential bulk stacking along (100), (110), and (111) directions, with interlayer distances, d_{\parallel} , of 0.287, 0.207, and 0.316 nm, respectively,¹ in line with other HR-TEM studies, which found a layer distance along (111) direction of 0.32 nm,⁷ 0.285 nm along the (100),⁶ and values of 0.33 and 0.28 nm for the (111) and (100) directions, respectively.¹¹ Note that experiments sometimes refer to a cation disordered

schapbachite $Fm\bar{3}m$ rocksalt structure, yet cation ordering is not observable by HR-TEM means, and only indirectly by changes in conductivity at high temperatures.¹³ Indeed, the matildite structure can be embedded within a $Fm\bar{3}m$ rocksalt type of structure, and so, misinterpreted as such, see below.

In any case, and similarly to other semiconductors, such as ZnO, different AgBiS₂ morphologies can be obtained depending on the nanoparticle production procedure and the present capping agents,¹⁴ including so far irregular nanoparticles, hexagonal prisms, nanostructured flowers, and nanorods of μm of length.^{11,15-17} The variety of conditions and capping agents, including passivation agents, and crosslinking molecules is out of the scope of the present research,^{1,11} which is first aimed at completely describing the structure and stability of the preferential surface terminations of pristine orderly structured matildite and the natural nanoparticle isolated morphology, enabling the posterior study of the interaction of solution molecules on them, including the morphology reshaping.

2. Surface models and computational details

The experimental crystallographic structure of matildite AgBiS₂ has been acquired (a trigonal based primitive unit cell with Pearson symbol $hP12$ and space group 164, *i.e.* $P\bar{3}m1$),¹⁸ known to be the responsible polymorph with photoelectronic response. However, for convenience, we used a cubic supercell $Fm\bar{3}m$ rocksalt alike, known and employed in the literature as D4, AFIIb, or alternate cation polymorphs.^{13,19-21} Note that, because of this choice, we use in the following the Miller notation instead of the Miller-Bravais notation. See in Figure 1 the matildite cubic bulk supercell, easily recognizable as a face-centred cubic arrangement of S atoms, in which Ag and Bi atoms insert in a NaCl fashion, being alternated in each of the three cell directions, where the $P\bar{3}m1$ structure can be embedded. Despite all $\{001\}$ planes are equivalent within the periodic boundary conditions, the cation alternation creates an anisotropy for the $\{011\}$ planes, and because of this, two possible terminations have been considered, named $(011)^I$ and $(011)^{II}$, see Figures 1 and 2. This anisotropy shows up for the $\{111\}$ planes, in which in one particular direction alternating planes of Bi and Ag exist, and consequently, two terminations are possible while maintaining the material stoichiometry: Either featuring endings containing only Bi or S, $(111)^I$, or containing only Ag or S, $(111)^{II}$, see Figures 1 and 2. In addition, other three $\{111\}$ directions

exist, in which the S ending combines with a bimetallic AgBi termination, (111)^{III}, see Figures 1 and 2.

Calculations have been carried out within the framework of DF theory using the Vienna *ab initio* simulation package VASP.²² Since the main target is the structure-energy relationship, calculations have been carried out using the Perdew-Burke-Ernzerhof (PBE) exchange-correlation (xc) functional,²³ a well-known member of the family of functionals issued from the generalized gradient approximation (GGA), and suited at correctly describing the energetic preference.^{10,13} The previously PBE optimized matildite bulk structure has been used as a kick-off structure, from which surfaces are simulated employing slab models with periodic boundary conditions. For details on the AgBiS₂ bulk optimization, we refer to the recent work in the literature.¹⁰

Surface slabs have been constructed by aligning the surface direction with the unit cell *c* axis, accounting for a given number of material layers, and adding, in all cases, a vacuum region of 10 Å, known to be sufficient to isolate slabs and to avoid interactions among translationally repeated slabs. Details of the employed slabs, including the number of AgBiS₂ structural units, *n*, the slab width, and the bulk interlayer spacing are contained in Table 1. Test calculations using thicker slabs delivered negligible variations in the bandgap below 0.05 eV. Note how the interlayer distances, *d*_{||}, are in excellent agreement with those recently reported, with deviations of at most 0.07 Å. Figure 2 depicts the supercell dimensions in *a* and *b* cell vectors, while Figure 3 shows a side view of them. Table 1 also contains Monkhorst-Pack²⁴ **k**-points meshes employed, adjusted to maintain the **k**-point density optimized for bulk matildite, where variations of that just succinctly modified the total energy with variations below 0.04 eV.

In the present calculations a plane-wave basis was used to represent the valence electronic density, with a kinetic energy cutoff of 415 eV. The effect of the core electrons in the valence electronic density has been taken into account using the projected augmented wave (PAW) method as implemented in VASP.^{25,26} Note in passing by that the PAW method is effectively all electron with a frozen core including scalar relativistic effects, especially important for heavy elements such as Ag or Bi. Atomic positions were allowed to fully relax until forces acting on atoms were below 0.01 eV Å⁻¹. Calculations were carried in a spin-polarized fashion, although the total

magnetic moments were found to be nominally zero, and so further analysis was carried out in a non spin-polarized manner. A tetrahedron method was used for the smearing, with an energy window of 0.1 eV, although final energies are extrapolated to 0 K. Atomic charges have been estimated through a Bader analysis.^{27,28}

Cleavage energies, E_{cl} , have been gained from the energy of the relaxed slab models, E_{slab} , as:

$$E_{cl} = \frac{E_{slab} - n \cdot E_{bulk}}{A} \quad (5)$$

where n is the number of AgBiS₂ units in the slab, E_{bulk} the energy of one bulk AgBiS₂ unit, and A the area of the exposed surface in the unit cell, see Figure 2. For slabs where both terminations are identical, the E_{cl} equals twice the surface energy, γ , of each ending. The relaxed E_{cl} values which are used to depict the Wulff construction optimal shape,^{29,30} employing the visualization for electronic and structural analysis (VESTA) package.³¹ The work function (ϕ) for the studied surfaces has been determined following the usual definition and equaling the difference between the energy of one electron in a vacuum and that of the Fermi energy (E_F).

Note in passing by that some of the modeled surfaces are polar, given that AgBiS₂ is a Type 3 solid according to Tasker classification.³² Because of this, the surface and cleavage energies of the pristine models diverge with the slab width. Diverse mechanism exist to nullify this electric dipole moment, which include charge transfer among the different polar endings, the surface reconstruction, the dipole quenching by molecular adsorption, and the appearance of surface vacancies. Likely these polar surfaces exist as here modeled either in small nanoparticles, where such charge transfer is likely, and the electric dipole moment instability is not acute, or in the case such surfaces are capped with molecules, as happens in ZnO polar surfaces.³³ Notice that other than these situations, a proper study on the polar surfaces reconstruction and/or vacancies formation and clusterization should be undertaken, which is, however, out of the scope of the present study purposes.

3. Results and discussion

The cleavage energies of the optimized surfaces are reported in Table 2. On one hand one has to first realize the small range involving these surface energies; they span a 0.5-1.8 J m⁻² range where other semiconductors such as ZnO feature values up to ~3 J

m^{-2} ,¹⁴ even up to $\sim 7 \text{ J m}^{-2}$ for molybdenum carbides, with mixed metallic-ionic bonds.³⁴ This can be taken as an indication of the feasibility of synthesizing small nanoparticles of AgBiS_2 compared to other materials. Furthermore, notice that for the polar (111) direction, the cut combining Ag and S endings, *i.e.* the $(111)^{\text{II}}$, is much more stable — 0.48 J m^{-2} — compared to the Bi and S endings — $(111)^{\text{I}}$, 1.37 J m^{-2} —, highlighting that the Ag-S bonds within matildite are much weaker than Bi-S ones, point that goes along with an easier Ag vacancy formation compared to Bi.¹³

Indeed, the $(111)^{\text{II}}$ surface is the one most stable from those explored here, even despite displaying polar endings, and actually naturally explains the Ag rich surface observation in nanoparticle samples.¹ The Wulff constructed shape acquired following the cleavage energies encompassed in Table 2 is depicted in Figure 4, and reveals that only (001) — E_{cl} of 0.52 J m^{-2} — and $(111)^{\text{II}}$ surfaces are exposed, *i.e.* the optimal Wulff shape is a cube featuring $\{001\}$ facets, with only two cuts along $(111)^{\text{II}}$ direction. According to it, a 84.81% of the nanoparticle surface would belong to the nonpolar $\{001\}$ facets, and the other sensible 15.19% would belong to the polar $(111)^{\text{II}}$ ending. With such a ratio of exposure, and noting that $\{001\}$ facets contain Ag, Bi, and S atoms, and that $(111)^{\text{II}}$ contain only Ag and S atoms in each of the two endings, one can estimate the surface atomic Ag:Bi ratio in Wulff shaped nanoparticles, which according to our estimates is 1.36, actually, in rather good agreement to the ratio obtained from X-ray photoemission spectroscopy (XPS) measurements in as-synthesized matildite nanoparticles of 1.5. Keeping that in mind, the easier Ag vacancy formation in bulk¹³ is then a sensible explanation for other studies where Ag poor samples were detected.^{11,35}

As far as local charges of surface atoms, results from a Bader analysis are reported in Table 2. It is worth noting how charges on (001) nonpolar surfaces are very similar to those previously calculated in bulk matildite, of +0.47, +1.21, and -0.83 e for Ag, Bi, and S, respectively, with variation of at most 0.08 e . In this sense, such termination is the most bulk-like. However, charges are sensibly attenuated on nonpolar $(011)^{\text{I}}$ and $(011)^{\text{II}}$ surfaces, with absolute reductions of 0.2-0.3 e compared to bulk conditions. This goes along with the above-commented charge-transfer mechanism, although the small charge transferred seems to point for a small electric dipole moment term. Regardless of that, the work functions of nonpolar surfaces are of $\sim 4.3 \text{ eV}$, and only higher by 0.32 eV on the more unstable $(011)^{\text{II}}$ surface, which highlights again the surface charge compensation in such nonpolar endings. This charge attenuation is of

similar extent on polar (111) endings, with reductions of 0.2-0.3 e for surface Ag and S atoms. However, the reduction is much higher for those (111) surfaces containing surface Bi atoms, these are the (111)^I and (111)^{III} surfaces. There, the high positive charged of Bi cations get reduced by $\sim 0.6 e$, although such a big reduction, probably a consequence of a charge transfer mechanism to reduce polarity,^{32,36} does not implies a particular stability, as such surfaces containing surface Bi atoms are the least stable of those here contemplated. For the studied polar surfaces, the work functions are higher than for the nonpolar ones, by in between 1.5 to 2.2 eV, regardless of the higher instability; clearly the dipole moment barrier is a factor when it comes to electron extraction. However, the polarity is not detrimental for the high stability for (111)^{II} Ag/S polar endings, where such surface dipole exists, though quenched, and despite of that is the most stable surface here contemplated, clearly preferable to the competing (111)^I Bi/S termination. In that sense, the Ag layer termination is much more stable than the Bi terminated one. Considering the above-commented Wulff ratios, the mean workfunction of a Wulff shaped AgBiS₂ nanoparticle would be 4.55 eV.

Finally, the surface density of states (DOS) is shown in Figure 5 as projected on surface atoms per studied surface. For the bulk reference, we refer to the recent literature.¹⁰ Note that for each surface the potential energy of an electron in the vacuum is used as the energy reference, E_V , instead of the usual Fermi level (E_F), which is then located at minus the workfunction energy value as listed in Table 2. From the DOS several conclusions can be extracted. For instance, the DOS of the nonpolar (001), (011)^I, and (011)^{II} surfaces quite resemble that of bulk matildite AgBiS₂,¹⁰ in the sense that valence band is dominated by Ag and S orbitals, whereas conduction band is dominated by Bi and S. Further than that, such surfaces display a bandgap. In the case of (001) surface, the bandgap E_g at surface is 0.72 eV, 0.3 eV larger than that of bulk estimated to be 0.42 eV at the same PBE level.

Such sensible enlargement of the bandgap, when applied to better estimates obtained using hybrid functionals, could account for the wavelength overestimation when simulating absorption coefficients, thus helping to reconcile computational simulations with experiments,¹⁻¹⁰ which here remarks the paramount role of (001) surface termination in solar light triggered processes. The (011)^I and (011)^{II} surfaces, not expressed in Wulff shapes, see Figure 4, feature reduced band gaps of 0.21 and 0.23 eV. Last but not least, polar (111) surfaces feature no band gap at all, *i.e.* these surface

terminations can be considered metallic. Particularly, the states near E_F are governed by S orbitals, mainly, and those above E_F by Bi states for $(111)^I$ and $(111)^{II}$ surfaces, and by Ag states in $(111)^{II}$ surface. Since E_F of the Wulff expressed $(111)^{II}$ surface with respect to the vacuum is located sensibly lower in energy to that of (001) surface, a photo-generated electron/hole pair on (001) surfaces could be followed by an electron transfer to the metallic $(111)^{II}$ surface, fostering charge separation which help to explain the better photoactive performance of matildite AgBiS_2 , as similarly previously found on other semiconductors as ZnO .¹⁴ This reasoning however has to be taken with caution, possible applicable to small nanoparticles, as size, and likely the presence of capping agents can revert such situation, recovering the bandgap at polar surfaces, points which should be the matter of future studies.

IV. Conclusions

Motivated by the interest in matildite AgBiS_2 material for solar light harvesting applications, we follow up a detailed bulk first principles quantum mechanical study by a through investigation of the surface morphology. DFT calculations carried out at the PBE level on different surface orientations and terminations highlight the likely presence of two particularly stable facets in Wulff shaped AgBiS_2 nanoparticles; the (001) type nonpolar surfaces, and (111) polar terminations where facets are exposed containing solely Ag or S atoms. Considering them the Wulff equilibrium shape is a cube with only two edges capped. This particular shape explains a previously experimentally determined surface enrichment of Ag with respect Bi of ~ 1.5 . The (001) surfaces display an ionic character similar to bulk AgBiS_2 , with a low work function of 4.31 eV, although the inspection of the DOS reveals a bandgap increased by 0.3 eV compared to those of bulk. Such surface increase could explain the bulk wavelength overestimation of the absorption coefficient decay, as previously determined. Last but not least, the DOS of (111) polar termination reveals a metal character, where Fermi level is located below that on the (001) surfaces. According to this, a possible $(001) \rightarrow (111)$ electron transfer of the (001) surface generated exciton could explain a hindered exciton recombination, and thus account for the excellent reported photoactivity.

Acknowledgements: This work has been supported by Spanish Ministry of Economy and Competitiveness (MINECO) and *Fondo Europeo de Desarrollo Regional* (FEDER) CTQ2015-64618-R and MAT2014-56210-R grants and partly by *Generalitat de Catalunya* grants 2014SGR97, 2014SGR1548, XRQTC and the *Fundación Privada Cellex*. The research in this work is in the framework of the NOMAD Center of Excellence project which received funding from the European Union's Horizon 2020 research and innovation programme under grant agreement N° 676580. F.V. thanks MINECO for a postdoctoral *Ramón y Cajal* (RyC) research contract (RYC-2012-10129). F.I. acknowledges additional support from the 2015 ICREA Academia Award for Excellence in University Research. G.K. acknowledges financial support from the European Research Council (ERC) under the European Union's Horizon 2020 research and innovation programme (grant agreement No 725165) and the Spanish Ministry of Economy and Competitiveness, through the *Severo Ochoa* Programme for Centres of Excellence in R&D (SEV-2015-0522).

Figure 1. Matildite bulk crystallographic structure, employing the cubic supercell (top image), with the explored surface orientations, and the embedded trigonal primitive unit cell (bottom image, highlighted atoms with red lines to guide the eyes). Grey, pink, and yellow spheres denote Ag, Bi, and S atoms, respectively.

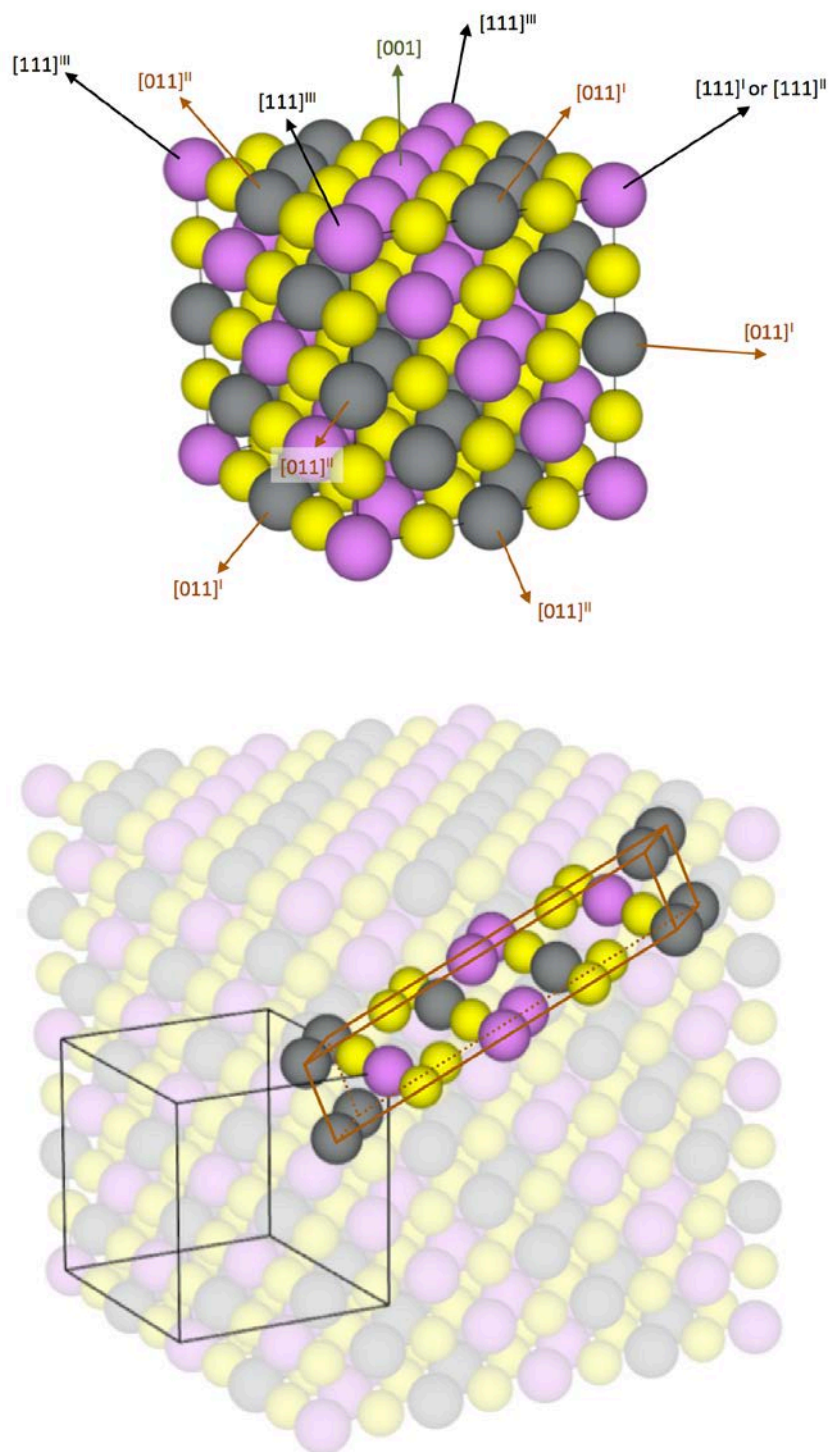


Figure 2. Top views of the matildite AgBiS_2 (001), $(011)^{\text{I}}$, $(011)^{\text{II}}$, $(111)^{\text{I}}$, $(111)^{\text{II}}$, and $(111)^{\text{III}}$ surfaces. Dashed white lines denote the surface unit cells employed. Atomic sphere coloring as in Figure 1.

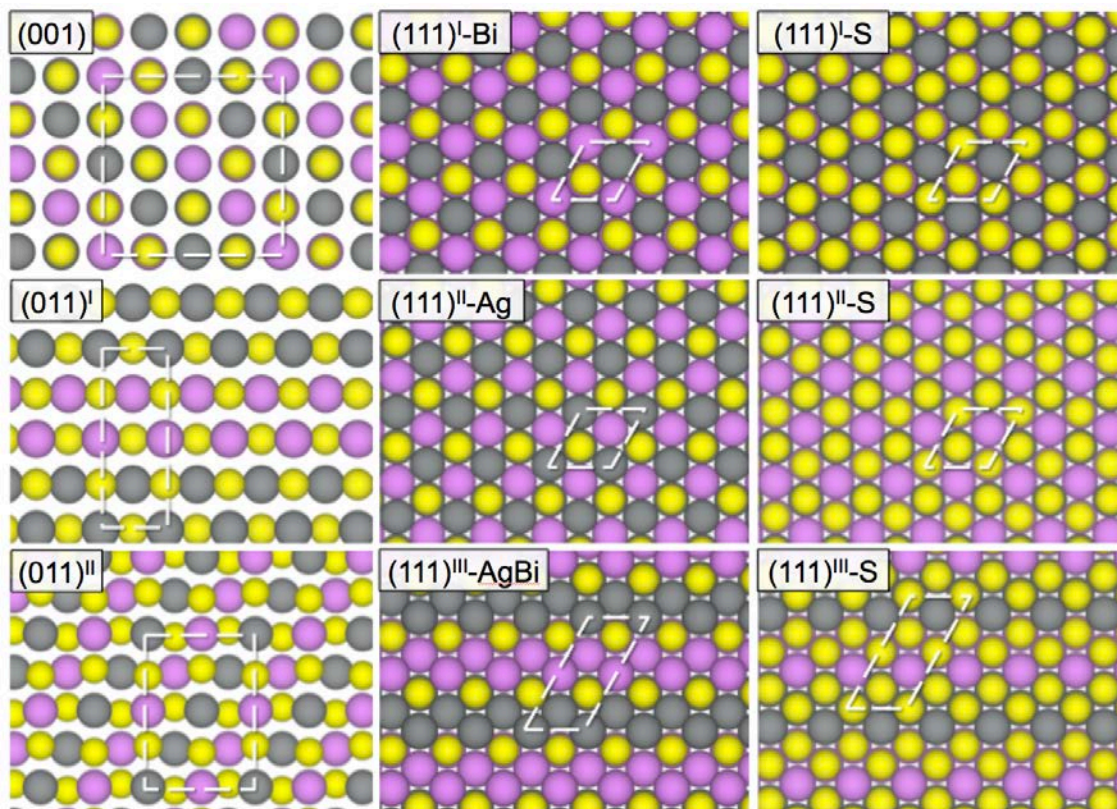


Figure 3. Side views of the matildite AgBiS_2 (001), $(011)^{\text{I}}$, $(011)^{\text{II}}$, $(111)^{\text{I}}$, $(111)^{\text{II}}$, and $(111)^{\text{III}}$ surfaces. Atomic sphere coloring as in Figure 1.

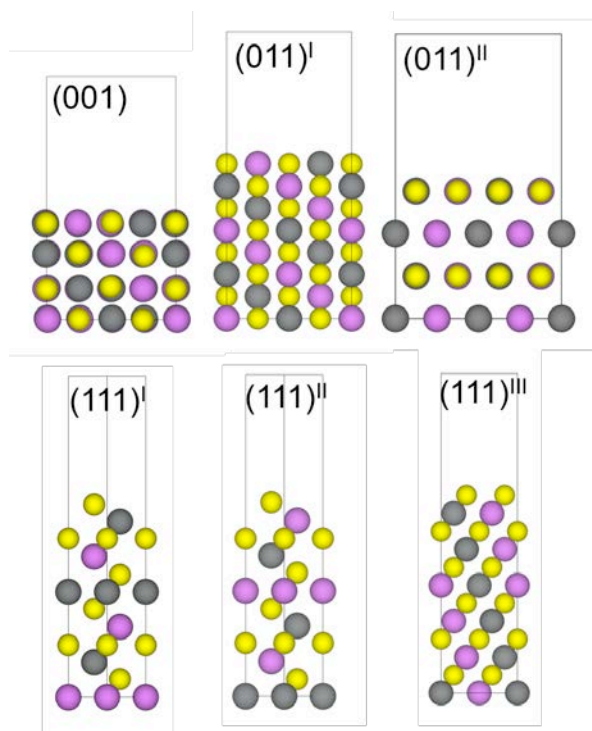


Figure 4. Wulff construction shaped gained from cleavage energies as computed and presented in Table 2.

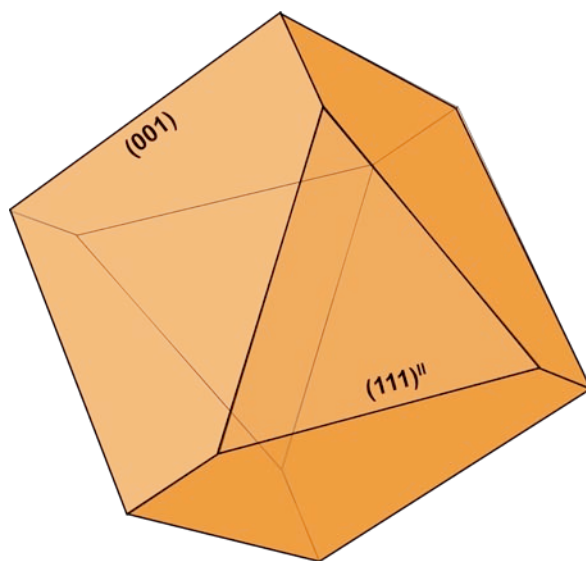


Figure 5. Atomic projected DOS for the studied surfaces, following the colour code of Figure 1, and referenced to the vacuum level (E_V), denoted by a dashed black line. For each surface, the Fermi energy, E_F , is marked with a solid red line.

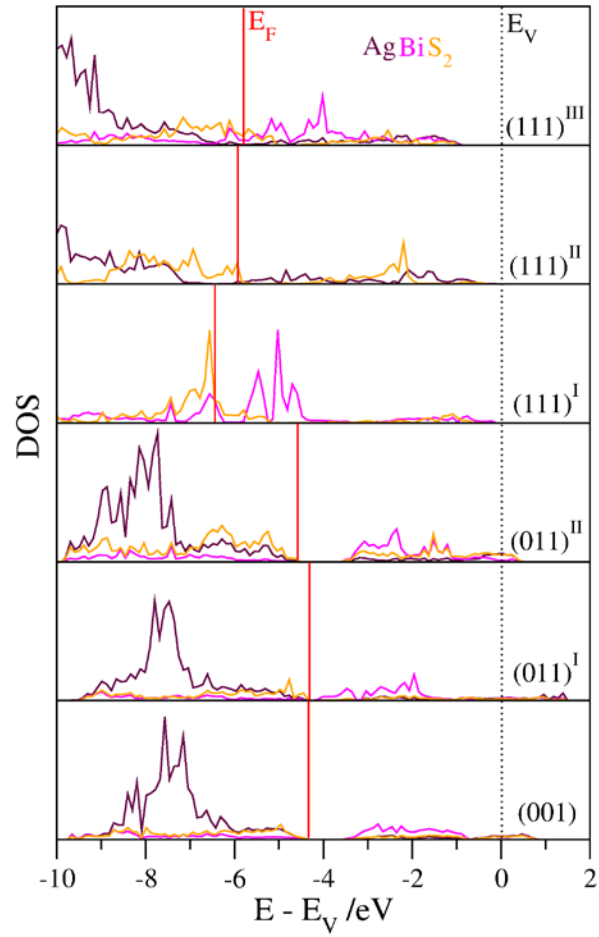


Table 1. Number of AgBiS₂ units, n , for each surface slab model, together with the slab width, in Å. Experimental (Exp.) and calculated (PBE) interlayer distances, d_{\parallel} , also in Å, and dimensions of the Monkhorst-Pack \mathbf{k} -point meshes.

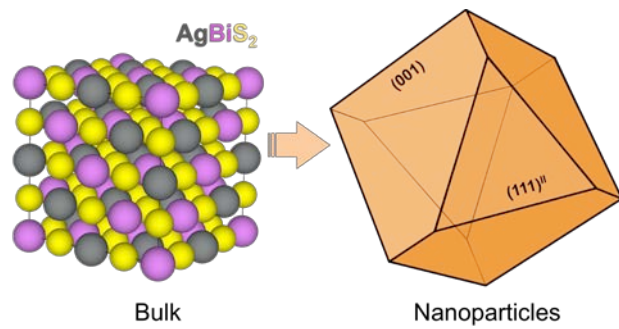
Surface	n	width	d_{\parallel}(PBE)	d_{\parallel}(Exp.)^a	\mathbf{k}-points
(001)	16	8.5	2.83	2.87	5×5×1
(011) ^I	8	14.0	2.00	2.07	9×3×1
(011) ^{II}	16	14.0	2.00	2.07	5×5×1
(111) ^I	3	17.5	3.18	3.16	9×9×1
(111) ^{II}	3	17.5	3.18	3.16	9×9×1
(111) ^{III}	3	17.5	3.18	3.16	9×9×1

^a Ref. 1.

Table 2. Cleavage energies, E_{cl} , in J m^{-2} , work functions, ϕ , in eV, and charge on surface atoms, Q , in e .

Surface	E_{cl}	ϕ	Q_{Ag}	Q_{Bi}	Q_{S}
(001)	0.52	4.31	+0.45	+1.29	-0.90
(011) ^I	0.90	4.30	+0.24	+0.91	-0.62
(011) ^{II}	1.14	4.63	+0.26	+1.03	-0.70
(111) ^I	1.37	6.47	–	+0.56	-0.34
(111) ^{II}	0.48	5.92	+0.31	–	-0.70
(111) ^{III}	1.76	5.79	+0.24	+0.61	-0.50

TOC Graphic



References:

- (1) Bernechea, M.; Miller, N.C.; Xercavins, G.; So, D.; Stavrinadis, A.; Konstantatos, G. Solution-processed Solar Cells Based on Environmentally Friendly AgBiS₂ Nanocrystals. *Nat. Photon.* **2016**, *10*, 521-525.
- (2) Guin, S.N.; Biswas, K. Cation Disorder and Bond Anharmonicity Optimize the Thermoelectric Properties in Kinetically Stabilized Rocksalt AgBiS₂ Nanocrystals. *Chem. Mater.* **2013**, *25*, 3225-3231.
- (3) Pejova, B.; Nesheva, D.; Aneva, Z.; Petrova, A. Photoconductivity and Relaxation Dynamics in Sonochemically Synthesized Assemblies of AgBiS₂ Quantum Dots. *J. Phys. Chem. C* **2011**, *115*, 37-46.
- (4) Guin, S.N.; Chatterjee, A.; Negi, D.S.; Datta, R.; Biswas, K. High Thermoelectric Performance in Tellurium Free *p*-type AgSbSe₂. *Energy Environ. Sci.* **2013**, *6*, 2603.
- (5) Xiao, C.; Qin, X.; Zhang, J.; An, R.; Xu, J.; Li, K.; Cao, B.; Yang, J.; Ye, B.; Xie, Y. High Thermoelectric and Reversible *p-n-p* Conduction Type Switching Integrated in Dimetal Chalcogenide. *J. Am. Chem. Soc.* **2012**, *134*, 18460-18466.
- (6) Huang, P.-C.; Yang, W.-C.; Lee, M.-W. AgBiS₂ Semiconductor-Sensitized Solar Cells. *J. Phys. Chem. C* **2013**, *117*, 18308-18314.
- (7) Guin, S.N.; Srihari, V.; Biswas, K. Promising Thermoelectric Performance in *n*-type AgBiSe₂: Effect of Aliovalent Anion Doping. *J. Mater. Chem. A* **2015**, *3*, 648-655.
- (8) Ma, J.; Delaire, O.; May, A.F.; Carlton, C.E.; McGuire, M.A.; VanBebber, L.H.; Abernathy, D.L.; Ehlers, G.; Hong, T.; Huq, A. *et al.* Glass-like Phonon Scattering from a Spontaneous Nanostructure in AgSbTe₂. *Nat. Nanotechnol.* **2013**, *8*, 445-451.
- (9) Welnic, W.; Wuttig, M. Reversible Switching in Phase-change Materials. *Mater. Today* **2008**, *11*, 20-27.
- (10) Viñes, F.; Bernechea, M.; Konstantatos, G.; Illas, F. Matildite Versus Schapbachite: First-principles Investigation of the Origin of Photoactivity in AgBiS₂. *Phys. Rev. B* **2016**, *94*, 235203.
- (11) Chen, C.; Qiu, X.; Ji, S.; Jia, C.; Ye, C. The Synthesis of Monodispersed AgBiS₂ Quantum Dots with a Giant Dielectric Constant. *CrystEngComm* **2013**, *15*, 7644-7648.

-
- (12) Nesheva, D.; Aneva, Z.; Pejova, B.; Grozdanov, I.; Petrova, A. Photoelectrical Characterization of Nanocrystalline AgBiS₂ Thin Films. *J. Optoelectron. Adv. M.* **2009**, *11*, 1347-1350.
- (13) Guin, S.N.; Banerjee, S.; Sanyal, D.; Pati, S.K.; Biswas, K. Origin of the Order–Disorder Transition and the Associated Anomalous Change of Thermopower in AgBiS₂ Nanocrystals: A Combined Experimental and Theoretical Study. *Inorg. Chem.* **2016**, *55*, 6323-6331.
- (14) Iglesias-Juez, A.; Viñes, F.; Lamiel-García, O.; Fernández-García, M.; Illas, F. Morphology Effects in Photoactive ZnO Nanostructures: Photooxidative Activity of Polar Surfaces. *J. Mater. Chem. A* **2015**, *3*, 8782-8792.
- (15) Liang, N.; Chen, W.; Dai, F.; Wu, X.; Zhang, W.; Li, Z.; Shen, J.; Huang, S.; He, Q.; Zai, J.; Fang, N.; Qian, X. Homogenously Hexagonal Prismatic AgBiS₂ Nanocrystals: Controlled Synthesis and Application in Quantum Dot-sensitized Solar Cells. *CrystEngComm* **2015**, *17*, 1902-1905.
- (16) Shen, G.; Chen, D.; Tang, K.; Qian, Y. Novel Polyol Route to AgBiS₂ Nanorods. *J. Cryst. Growth* **2003**, *252*, 199-201.
- (17) Yan, J.; Yu, J.; Zhang, W.; Li, Y.; Yang, X.; Li, A.; Yang, X.; Wang, W.; Wang, J. Synthesis of Cu₃BiS₃ and AgBiS₂ Crystallites with Controlled Morphology Using Hypocrellin Template and their Catalytic Role in the Polymerization of Alkylsilane. *J. Mater. Sci.* **2012**, *47*, 4159-4166.
- (18) Bayliss, P. Crystal Chemistry and Crystallography of Some Minerals in the Tetradymite Group. *Amer. Mineral.* **1991**, *76*, 257-265.
- (19) Hoang, K.; Mahanti, S.C.; Salvador, J.R.; Kanatzidis, M.G. Atomic Ordering and Gap Formation in Ag-Sb-Based Ternary Chalcogenides. *Phys. Rev. Lett.* **2007**, *99*, 156403.
- (20) Geller, S.; Wernick, J.H. Ternary Semiconducting Compounds with Sodium Chloride-like Structure: AgSbSe₂, AgSbTe₂, AgBiS₂, AgBiSe₂. *Acta Crystallogr.* **1959**, *12*, 46-54.
- (21) Barabash, S.V.; Ozolins, V. Order, Miscibility, and Electronic Structure of Ag(Bi,Sb)Te₂ Alloys and (Ag,Bi,Sb)Te Precipitates in Rocksalt Matrix: A First-principles Study. *Phys. Rev. B* **2010**, *81*, 075212.
- (22) Kresse G.; Furthmüller, J. Efficient Iterative Schemes for *Ab Initio* Total-energy Calculations Using a Plane-wave Basis Set. *Phys. Rev. B* **1996**, *54*, 11169.

-
- (23) Perdew, J.P.; Burke, K.; Ernzerhof, M. Generalized Gradient Approximation Made Simple. *Phys. Rev. Lett.* **1996**, *77*, 3865.
- (24) Monkhorst H.J.; Pack, J.D. Special Points for Brillouin-zone Integrations. *Phys. Rev. B* **1976**, *13*, 5188.
- (25) Blöchl, P.E. Projector Augmented-wave Method. *Phys. Rev. B* **1994**, *50*, 17953.
- (26) Kresse, G.; Joubert, D. From Ultrasoft Pseudopotentials to the Projector Augmented-wave Method. *Phys. Rev. B* **1999**, *59*, 1758.
- (27) Henkelman, G.; Arnaldsson, A.; Jónsson, H. A Fast and Robust Algorithm for Bader Decomposition of Charge Density. *Comput. Mater. Sci.* **2006**, *36*, 354-360.
- (28) Bader, R.F. *Atoms in Molecules: A Quantum Theory*, Oxford Science, Oxford, UK, **1990**.
- (29) Viñes, F.; Gomes J.R.B.; Illas, F. Understanding the Reactivity of Metallic Nanoparticles: Beyond the Extended Surface Model for Catalysis. *Chem. Soc. Rev.* **2014**, *43*, 4922-4939.
- (30) Barmparis, G.D.; Lodziana, Z.; Lopez, N.; Remediakis, I.N. Nanoparticle Shapes by Using Wulff Constructions and First-principles Calculations. *Beilstein J. Nanotechnol.* **2015**, *6*, 361–368.
- (31) Momma K.; Izumi, F. VESTA 3 for Three-dimensional Visualization of Crystal, Volumetric and Morphology Data. *J. Appl. Crystallogr.* **2011**, *44*, 1272-1276.
- (32) Noguera, C.; Goniakowski, J. Polarity in Oxide Nanoobjects. *Chem. Rev.* **2013**, *113*, 4073-4105.
- (33) Viñes, F.; Iglesias-Juez, A.; Illas, F.; Fernández-García, M. Hydroxyl Identification on ZnO by Infrared Spectroscopies: Theory and Experiments. *J. Phys. Chem. C* **2014**, *118*, 1492–1505.
- (34) Politi, J.R.D.S.; Viñes, F.; Rodriguez J.A.; Illas, F. Atomic and Electronic Structure of Molybdenum Carbide Phases: Bulk and Low Miller-index Surfaces. *Phys. Chem. Chem. Phys.* **2013**, *15*, 12617.
- (35) Nakamura, M.; Nakamura, H.; Ohsawa, T.; Imura, M.; Shimamura, K.; Ohashi, N. AgBiS₂ Single Crystal Grown Using Slow Cooling Method and its Characterization. *J. Cryst. Growth* **2015**, **411**, 1-3.
- (36) Goniakowski, J.; Finocchi, F.; Noguera, C. Polarity of Oxide Surfaces and Nanostructures. *Rep. Prog. Phys.* **2008**, *71*, 016501.